Chemical Engineering Science 119 (2014) 30–39

Contents lists available at ScienceDirect

Chemical Engineering Science

journal homepage: www.elsevier.com/locate/ces

Crystal shape and size control using a plug flow crystallization configuration

Joseph Sang-Il Kwon [a], Michael Nayhouse [a], Gerassimos Orkoulas [a], Panagiotis D. Christofides [a,b,*]

[a] Department of Chemical and Biomolecular Engineering, University of California, Los Angeles, CA 90095, USA
[b] Department of Electrical Engineering, University of California, Los Angeles, CA 90095, USA

HIGHLIGHTS

- Dynamic modeling of the evolution of crystal shape and size in continuous plug flow crystallization.
- Simulation and optimization of operating conditions.
- Feed disturbance handling with feed-forward control in plug flow crystallization.
- Simulation results exemplify shape control of lysozyme protein crystals of different feed seed distributions.

ARTICLE INFO

Article history:
Received 14 April 2014
Received in revised form
4 July 2014
Accepted 29 July 2014
Available online 6 August 2014

Keywords:
Protein crystallization
Continuous plug flow crystallizer
Kinetic Monte Carlo simulation
Process optimization
Process modeling
Process control

ABSTRACT

This work focuses on modeling and control of a continuous plug flow crystallizer (PFC) used to produce tetragonal hen-egg-white (HEW) lysozyme crystals and proposes an optimization-based control scheme to produce crystals with desired size and shape distributions in the presence of disturbances. Initially, a kinetic Monte Carlo (kMC) model is developed to simulate the crystal growth in a seeded PFC, which consists of five distinct segments. The crystal growth rate equations taken from (Durbin and Feher, 1986) are used in the kMC simulations for the modeling of the crystal growth in the direction of (110) and (101) faces. Then, a population balance equation (PBE) is presented to describe the spatio-temporal evolution of the crystal volume distribution of the entire crystal population, and the method of moments is applied to derive a reduced-order moment model. Along with the mass and energy balance equations, the leading moments that describe the dominant dynamic behavior of the crystal volume distribution are used in the optimization-based controller to compute optimal jacket temperatures for each segment of the PFC and the optimal superficial velocity, in order to minimize the squared deviation of the average crystal size and shape from the set-points throughout the PFC. Furthermore, a feed-forward control (FFC) strategy is proposed to deal with feed flow disturbances that occur during the operation of the PFC. Using the proposed optimization and control schemes, crystals with desired size and shape distributions are produced in the presence of significant disturbances in the inflow solute concentration and size distribution of seed crystals.

1. Introduction

Crystallization plays an essential role in the context of separation and purification methods for the production of therapeutic drugs. Considering the fact that crystal size and shape distributions have significant influence on the bioavailability of drugs such as the dissolution rate, filterability, and stability as a carrier to the target site, it becomes of particular interest to the pharmaceutical industry to produce crystals with desired size and shape distributions (Patience and Rawlings, 2001; Yang et al., 2006; Wang et al., 2008).

Traditionally, batch crystallization processes have been widely used in the pharmaceutical industry. However, the batch process has a few well-known potential drawbacks such as the batch-to-batch variability, and the difficulty in the scale-up and the consistent production of crystals with desired crystal size and/or shape distributions. Motivated by this, a mixed suspension mixed product removal (MSMPR) crystallization process, which is analogous to the conventional continuously stirred tank crystallizer

* Corresponding author at: Department of Chemical and Biomolecular Engineering, University of California, Los Angeles, CA 90095 USA. Tel.: +1 310 794 1015; fax: +1 310 206 4107.
E-mail address: pdc@seas.ucla.edu (P.D. Christofides).

http://dx.doi.org/10.1016/j.ces.2014.07.058
0009-2509/

(CSTC), has received a growing attention, and many efforts have been made in order to produce crystals from the MSMPR process with a higher production rate and desired product quality (Griffin et al., 2010; Alvarez et al., 2011; Hou et al., 2014; Ferguson et al., 2014). However, due to the presence of back-mixing, which is commonly modeled by employing the residence time mixing model, those crystals nucleated at a later stage during the crystallization process will reside a relatively short amount of time in the crystallizer and thus they will end up leaving the crystallizer with undesired size and shape distributions (Kwon et al., 2014). To this end, plug flow crystallizer (PFC) has been proposed to produce crystals with narrow size and shape distributions (Eder et al., 2011; Vetter et al., 2014).

More specifically, a strategy for the fines removal in the PFC was proposed through the manipulation of the growth and dissolution rates (Majumder and Nagy, 2013). Furthermore, the effect of the antisolvent injections along the axial direction of the PFC on the crystal volume distribution has been investigated (Alvarez and Myerson, 2010; Ferguson et al., 2013; Ridder et al., 2014).

Model-free control schemes such as a proportional-integral-derivative (PID) control scheme and a direct nucleation control approach are not able to handle alone constraints on the inputs, the outputs, and the rate of change of inputs while computing optimal jacket temperature values. Therefore, the necessity of incorporating the constraints to account for the physical limitations on the manipulated inputs and operating conditions makes the model-based control strategy (Miller and Rawlings, 1994; Worlitschek and Mazzotti, 2004; Shi et al., 2005; Mesbah et al., 2010) the method of choice for crystal size distribution control. Specifically, the model predictive control (MPC) scheme was employed by Kalbasenka et al. (2007) and Kwon et al. (2013, 2014, in press) in order to control the crystal size and shape distributions along with the consideration of the crystal growth and nucleation processes in both batch and MSMPR processes based on a reduced-order model. Furthermore, in addition to model-based optimization to compute optimal jacket temperature values, a feed-forward control (FFC) is proposed in the present work for the production of crystals with desired size and shape distributions owing to its unique ability to deal with feed flow disturbances that occur during the operation of the PFC though the use of the online measurements of the inflow solute concentration, PFC temperature, and crystal seed size.

In the pharmaceutical industry, disturbances (e.g., changes in the inflow solute concentration) influence the size and shape distributions of the crystal products during the steady-state operation of the PFC process (Sen et al., 2014). However, the conventional operating strategy such as the constant supersaturation control (CSC) scheme is not able to deal with the disturbances because it is not able to predict the spatio-temporal transient behavior of the system in response to disturbances in the inflow solute concentration and the seed size distribution.

Motivated by the above considerations, this work focuses on modeling and control of a continuous PFC used to produce tetragonal HEW lysozyme crystals and proposes an optimization-based control scheme to produce crystals with desired size and shape distributions in the presence of feed disturbances. Initially, we model a continuous plug flow crystallizer with 5 segments for the production of lysozyme crystals through kinetic Monte Carlo (kMC) simulation methods in the way described in Kwon et al. (2013) using the rate equations originally developed by Durbin and Feher (1991). A seeding strategy is used to decouple the nucleation from the crystal growth processes (Liu et al., 2010; Eder et al., 2011; Besenhard et al., 2014; Ferguson et al., in press). Furthermore, an upper bound of the supersaturation level is imposed as a constraint so that the system is enforced to stay in the metastable regime where the degree of primary nucleation is negligible (Shi et al., 2005). Then, a population balance equation (PBE) is presented to describe the spatio-temporal evolution of the crystal volume distribution, and by applying the method of moments to the PBE, a reduced-order moments model is derived because kMC models are not available in a closed form (Kalani and Christofides, 2002; Cogoni et al., 2014). Together with the mass and energy balance equations, the leading moments are used for the estimation of the spatio-temporal evolution of the crystal size and shape distributions in an optimization problem. Specifically, the crystallizer jacket temperatures at each segment and the superficial flow velocity are chosen as the decision variables in the optimization problem and the objective function is defined by the sum of the squared deviation of the average crystal size and shape from desired set-points throughout the PFC. Subsequently, the dynamic model developed in Section 2 is used for the design of an FFC strategy for the production of crystals with desired size and shape distributions properly suppressing the undesired effect caused by disturbances (Gnoth et al., 2007). Lastly, the simulation results are presented followed by discussion and conclusions.

2. Modeling of plug flow crystallizer

2.1. Process configuration

We consider a continuous plug flow crystallizer used to produce crystals with desired size and shape distributions through the manipulation of a set of jacket temperatures and of the superficial flow velocity which are computed by solving a multivariable optimization problem. The system parameters for the crystallizer considered in this work are taken from Alvarez and Myerson (2010) and Majumder and Nagy (2013), and are presented as follows: each segment of the PFC is 400 cm in length and 1.27 cm in inner diameter, and the PFC consists of 5 segments where the configuration of the PFC is presented in Fig. 1. It is assumed that the segments are connected without any gap. Additionally, we assume that the PFC is perfectly mixed in the radial direction and there is no back-mixing in the axial direction.

In order to study the effect of a set of jacket temperatures on the shape and size distributions of crystals produced by the plug flow crystallizer, it is operated in the regime where the primary nucleation is negligible. Therefore, a number of seed crystals with

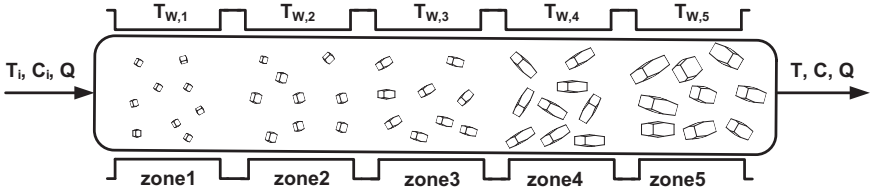

Fig. 1. Plug flow crystallizer configuration. T is the crystallizer temperature, T_i is the inflow temperature, $T_{w,k}$ is the crystallizer jacket temperature at segment k, C_i is the inflow solute concentration, C is the solute concentration, and Q is the flow rate of the inflow stream.

a height of 30 μm in both the direction of the (110) and (101) faces are fed through the entrance of the crystallizer. Specifically, the kMC simulations are used to simulate the crystal growth in the plug flow crystallizer described above. The crystal growth rates obtained from the kMC simulations are calibrated with literature data (Durbin and Feher, 1986). Additionally, the kMC simulations can be used to predict the crystal growth dynamics at the operating conditions where experimental data are not currently available. The details of the kMC simulations for the growth of the tetragonal lysozyme crystal, the basic assumptions and the rate equations for the microscopic processes (adsorption, desorption and migration) have been discussed extensively in the previous work (Kwon et al., 2013) and will not be repeated here.

During the PFC simulations, crystals are seeded at a rate of B_{seed} and travel along the PFC at the flow velocity until they exit the final segment. During this time the kMC simulations (Kwon et al., 2013) are used to model the crystal growth depending on the local environment at the current location of the crystal. Each segment of the PFC has 80 sections where the solute phase properties are considered to be constant and an upwind finite difference method is used to update the solute concentration and temperature values every 0.333 s. It is noted that a variable number of sections were tested to ensure stability of the finite difference method.

2.2. Mass balance

The mass balance employed in this work to compute the spatio-temporal evolution of the solute concentration becomes as follows:

$$\frac{\partial C}{\partial t} = -v_z\frac{\partial C}{\partial z} - \rho_c \int_0^\infty G_{vol}(V,\sigma)n(V,z,t)\,dV \tag{1}$$

where $n(V,z,t)$ is the number distribution of lysozyme crystals and is a function of crystal volume V, and of the position $z \in [0,L]$ in the axial direction at time t, L is the length of the reactor, v_z is the superficial flow velocity of the incoming flow into the axial direction, $C(z,t)$ is the protein solute concentration in the continuous phase, $\rho_c = 1400\ \mathrm{mg/cm^3}$ is the crystal density, and $\sigma = \ln(C/s)$ is the relative supersaturation where s mg/mL is the solubility. The solubility depends on temperature T, the pH of the solution, and the concentration of added electrolyte. At 4%(w/v) NaCl and pH=4.5, Cacioppo and Pusey (1991) represented the experimental solubility data as a function of temperature T in Celsius with the following 3rd-order polynomial:

$$s(T) = 2.88\times10^{-4}T^3 - 1.65\times10^{-3}T^2 + 4.62\times10^{-2}T + 6.01\times10^{-1}. \tag{2}$$

Alternatively, since the saturated liquid solution is sufficiently dilute in protein, the experimental solubility data at 4%(w/v) NaCl and pH=4.5 can be fitted with the following van't Hoff type of formula:

$$\ln(s) = \frac{\Delta H_c}{R}\left(\frac{1}{T+273.15}\right) + c. \tag{3}$$

Linear regression gives $c=27.45$ and $\Delta H_c = -4.5$ kJ/kg for the enthalpy of crystallization, which is in good accord with experiments (Schall et al., 1996). For modeling and control purposes, the polynomial representation, Eq. (2), that gives the same results as van't Hoff equation in the operating range of interest, is used in this work. Additionally, $G_{vol}(V,\sigma)$ is the volumetric crystal growth rate, which can be calculated as follows:

$$G_{vol}(V,\sigma) = 2G_{110}\langle h_{101}\rangle + G_{101}\langle h_{110}\rangle^2 \tag{4}$$

where $\langle h_{110}\rangle$ and $\langle h_{101}\rangle$ are the average crystal heights in the direction of (110) and (101) faces, respectively, and G_{110} and G_{101} are the crystal growth rates in the direction of (110) and (101) faces, respectively, where the geometry of the HEW lysozyme crystals considered in this work is presented in Fig. 2. The kMC simulations produce a dense grid of points of the growth rates for both (110) and (101) faces as a function of σ and thus, for a given σ, the value of the growth rate for each is obtained from interpolation. Lastly, Eq. (1) is subject to an initial condition at $t=0$ and a boundary condition at $z=0$ as follows:

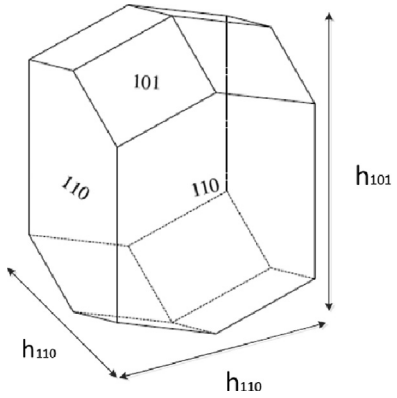

Fig. 2. Figure of HEW lysozyme crystal.

$$\begin{aligned} C(z,0) &= C_i \\ C(0,t) &= C_i \end{aligned} \tag{5}$$

where C_i is the inflow concentration and initial concentration of the PFC.

Remark 1. In this work, the HEW lysozyme protein is chosen because it is one of the most widely studied proteins, and thus there are available a number of experimental data in the literature for the nucleation and crystal growth rates of HEW lysozyme protein crystals. The proposed control scheme can be applied to other plug flow crystallization systems provided that experimental data for the crystal nucleation and growth rates are available.

2.3. Energy balance

Similar to the mass balance equation, the spatio-temporal evolution of the crystallizer temperature can be obtained by solving the following energy balance equation:

$$\frac{\partial T}{\partial t} = -v_z\frac{\partial T}{\partial z} - \frac{\rho_c \Delta H_c}{\rho C_p}\int_0^\infty G_{vol}(V,\sigma)n(V,z,t)\,dV - \frac{U_c a_c}{\rho C_p}(T - T_{w,k}) \tag{6}$$

where T is the crystallizer temperature, a_c is the heat transfer area per unit volume $(4/D)$ where D is the inner diameter of the plug flow crystallizer, $T_{w,k}$ is the crystallizer jacket temperature of the kth segment, $\Delta H_c = -4.5$ kJ/kg is the enthalpy of crystallization (Schall et al., 1996), $\rho(z,t) = 1000 + C(z,t)\ \mathrm{mg/cm^3}$ is the suspension density, $C_p = 4.13$ kJ/K kg is the specific heat capacity, and $U_c = 500\ \mathrm{kJ/m^2\,h\,K}$ is the overall heat transfer coefficient of crystallizer wall. Due to the small value of the enthalpy of crystallization, the term associated with latent heat effects in Eq. (6) has negligible contribution to the rate of change of temperature. Furthermore, Eq. (6) is subject to an initial condition at $t=0$ and a boundary condition at $z=0$ as follows:

$$\begin{aligned} T(z,0) &= T_i \\ T(0,t) &= T_i \end{aligned} \tag{7}$$

where T_i is the inflow temperature and initial temperature of the PFC.

2.4. Population balance equation

The population balance describing the spatio-temporal evolution of the crystal volume distribution for the PFC processes with

seeding can be written in the form of the following equation:

$$\frac{\partial n(V,z,t)}{\partial t}+v_z\frac{\partial n(V,z,t)}{\partial z}+\frac{\partial(G_{vol}(V,\sigma)n(V,z,t))}{\partial V}=B_{seed}\delta(V-V_0,z-z_0) \tag{8}$$

where B_{seed} is the seeding rate, $\delta(\cdot)$ is the Dirac delta function and V_0 is the size of the crystal seed. The term $v_z\partial n(V,z,t)/\partial z$ corresponds to the transport of crystals due to convection, and $\partial(G_{vol}(V,\sigma)n(V,z,t))/\partial V$ corresponds to the crystal growth.

2.5. Method of moments

By applying the method of moments to Eq. (8), we derive moment models that allow us to compute the spatio-temporal evolution of the number of crystals (i.e., zeroth moment M_0) and the total volume (i.e., first moment M_1) of crystals in the PFC processes. The jth moment equation has the following form:

$$\frac{\partial M_j}{\partial t}=-v_z\frac{\partial M_j}{\partial z}+jG_{vol}M_{j-1} \tag{9}$$

where we define the jth moment as $M_j(z,t)=\int_0^\infty V^j n(V,z,t)\,dV$. For the derivation of the moment model, refer to Appendix A.

3. Steady-state model

Initially, we study the behavior of the PFC process at steady state. The steady-state mass and energy balance equations, and the steady-state population balance equation, are obtained by setting the accumulation terms in Eqs. (1), (6), and (8) equal to zero. The population balance equation at steady state is a one-dimensional hyperbolic partial differential equation (PDE) and thus suggests the use of the method of characteristics for the computation of its solution, which will transform Eq. (8) to two ordinary differential equations (ODEs) of the crystal location, z, and of the crystal volume distribution, V, along the characteristic line (cf. Eq. (B.3)). As a result, it is derived in Appendix B that a spatial profile of the average volume distribution is described as

$$\frac{dV}{dz}=\frac{G_{vol}}{v_z}$$

3.1. Moment models

Specifically, the zeroth moment ($j=0$) of the moment model, Eq. (9), at steady state is as follows:

$$0=-v_z\frac{dM_0}{dz} \tag{10}$$

Thus, it follows that $M_0(z)$ is an explicit function of z:

$$M_0(z)=M_0(0) \tag{11}$$

where $M_0(0)$ is the number of seed crystals fed to the plug flow crystallizer through the entrance at steady state. This result is expected due to the lack of nucleation, aggregation, or breakage in the PFC process.

3.2. Spatial profiles at steady state

The spatial profiles of both the solute concentration and the crystallizer temperature are derived in Appendix C. Specifically, the solute concentration $C(z)$ at steady state is as follows:

$$C(z)=C_i-\frac{\rho_c G_{vol}M_0(0)}{v_z}z$$

Furthermore, the crystallizer temperature $T(z)$ at steady state is obtained as follows:

$$T(z)=\left(T_{w,k}-\frac{A}{B}\right)(1-e^{-Bz})+T_i e^{-Bz}$$

where $A=\rho_c\Delta H_c G_{vol}M_0(0)/\rho C_p v_z$ and $B=U_c a_c/\rho C_p v_z$

Remark 2. The transient solution obtained from the dynamic model has been computed and has been found to converge to the steady-state profile obtained from the steady-state model for a sufficiently large time and for the same set of parameters.

4. Multivariable optimization problem formulation

In this section, we propose a multivariable optimization problem (MOP), which will be solved in order to compute a set of optimal crystallizer jacket temperatures and the superficial flow rate for the multi-segment PFC to produce crystals with desired size and shape distributions. To this end, an objective function is defined by the sum of squared errors of the average crystal size, $(\langle V(z,t)\rangle-V_{set})^2$, and shape, $(\langle\alpha(z,t)\rangle-\alpha_{set})^2$, of the crystals throughout the PFC from the desired set-point values. In particular, $\langle\alpha(z,t)\rangle$ is the average crystal shape which is defined by the ratio between the average crystal heights in the direction of (110) and (101) faces throughout the PFC as follows: $\langle\alpha(z,t)\rangle\approx\langle h_{110}(z,t)\rangle/\langle h_{101}(z,t)\rangle$. The average crystal shape is approximated by these expressions in order to make use of $\langle h_{110}\rangle$ and $\langle h_{101}\rangle$ which are available through the real-time online measurements as is shown in Kwon et al. (2014). The decision variables are the jacket temperatures at each segment of the PFC $(T_{w,1},T_{w,2},T_{w,3},T_{w,4},T_{w,5})$ and the superficial flow velocity, v_z. A constraint on the range of the crystallizer temperature is imposed $4\,^\circ\text{C}\le T(z,t)\le 25\,^\circ\text{C}$ to make sure that the model protein remains in a proper condition for crystal growth. Note that the growth rate expressions, G_{110} and G_{101}, used in the MOP below are calibrated in Kwon et al. (2013) with the experimental data of Durbin and Feher (1986) for $2.1\le\sigma\le 4.1$ and is presented in Fig. 3. We want to note that the constraint (cf. $\sigma(z,t)\le 2.6$) in Eq. (12) is chosen in this range. Additionally, the inflow temperature, T_i, is set to be 18 °C.

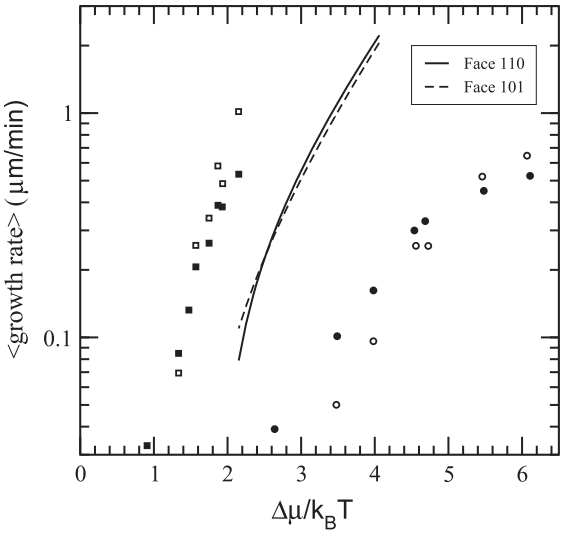

Fig. 3. The solid and dashed lines show the growth rates for the kMC model on the (110) and (101) faces, respectively, at $C=45$ mg/mL and 4% NaCl. The (•) and (○) represent, respectively, the growth rates for (101) and (110) faces with 3.5% NaCl and the (■) and (□) represent the growth rates with 5% NaCl at pH = 4.6, which both are taken from Durbin and Feher (1986).

The resulting optimization problem is as follows:

$$\underset{T_{w,1},T_{w,2},T_{w,3},T_{w,4},T_{w,5},v_z}{\text{Minimize}} \quad \sum_{t=1}^{t_f}\sum_{z=1}^{L} w_1(\langle\alpha(z,t)\rangle-\alpha_{\text{set}})^2+w_2(\langle V(z,t)\rangle-V_{set})^2$$

subject to

$$G_{110}=0.1843\times\sigma^3-1.1699\times\sigma^2+2.8885\times\sigma-2.5616$$

$$G_{101}=0.1893\times\sigma^3-1.2264\times\sigma^2+2.9887\times\sigma-2.5348$$

$$4\ ^\circ\text{C}\le T\le 25\ ^\circ\text{C}, \sigma(z,t)\le 2.6$$

$$\frac{\partial M_0}{\partial t}=-v_z\frac{\partial M_0}{\partial z}$$

$$\frac{\partial M_1}{\partial t}=-v_z\frac{\partial M_1}{\partial z}+G_{vol}M_0$$

$$\frac{\partial C}{\partial t}=-v_z\frac{\partial C}{\partial z}-\rho_c\frac{\partial M_1}{\partial t}$$

$$\frac{\partial T}{\partial t}=-v_z\frac{\partial T}{\partial z}-\frac{\rho_c\Delta H_c}{\rho C_p}\frac{\partial M_1}{\partial t}-\frac{U_c a_c}{\rho C_p}(T-T_{w,k})$$

$$G_{vol}=2G_{110}\langle h_{101}\rangle\langle h_{110}\rangle+G_{101}\langle h_{110}\rangle^2,\quad k\in\{1,2,3,4,5\}$$

$$\frac{d\langle h_i\rangle}{dz}=\frac{G_i}{v_z},\quad i\in\{110,101\}$$

$$\langle\alpha(z,t)\rangle\approx\frac{\langle h_{110}(z,t)\rangle}{\langle h_{101}(z,t)\rangle},\quad \langle V(z,t)\rangle=\langle h_{110}(z,t)\rangle^2\langle h_{101}(z,t)\rangle \tag{12}$$

where the weighting coefficients of the two objective function terms, w_1 and w_2, are determined by trial and error until the optimal jacket temperatures and the superficial flow velocity drive both size and shape distributions of the crystal products to a set of desired values. Furthermore, the supersaturation level is defined as the logarithmic difference between the solute concentration level and the solubility, $\sigma(z,t)=\ln(C(z,t)/s(z,t))$, and t_f is the total simulation time. A range of supersaturation is provided as a constraint (cf. $\sigma(z,t)\le 2.6$) in Eq. (12) to prevent the primary nucleation of crystals during the process. The corresponding range of the average crystal shape is $\langle\alpha\rangle\le 1.05$. The polynomial expressions for the growth rates G_{110} and G_{101} are obtained from open-loop simulations in Kwon et al. (2014). The forward upwind (FU) discretization scheme, which guarantees the stability of the system if the time and spatial discretization steps are relatively small (Graham and Rawlings, 2013), is applied to the moment models and the mass and energy balance equations in the MOP (cf. Eq. (12)) to evaluate spatio-temporal evolution of the system variables. Then, a set of optimal jacket temperatures and the superficial flow velocity ($T_{w,1}$, $T_{w,2}$, $T_{w,3}$, $T_{w,4}$, $T_{w,5}$, v_z) is obtained by solving Eq. (12) offline, and is applied to the crystallizer. We observed that the computational time needed to solve the optimization problem using the moments model is about 5–10 s. Therefore, if real-time measurements of crystallizer outlet stream are available with a reasonable sampling time, the proposed method can be applied to an experimental plug flow crystallization system. In general, the computational time and the convergence of the solution computed from an optimization problem depend on the integration step used to solve the moments model and thus it should be chosen carefully to obtain an accurate solution meeting real-time computational requirements.

Remark 3. The growth rates of the HEW lysozyme in the direction of (110) and (101) faces used in the simulations presented in the paper have been calibrated with available experimental results. However, no experimental results are currently available for the production of HEW lysozyme crystals through PFC. We note that the proposed optimization and control framework can be applied to other plug flow crystallization systems provided that the modeling, measurement, and computational requirements needed to implement the proposed approach in a practical setting are satisfied.

5. Feed-forward control

In continuous crystallization processes, disturbances (e.g., changes in the inflow solute concentration) influence the size and shape distributions of the crystal products during the steady-state operation of the PFC process (Sen et al., 2014). Motivated by this, the following feed-forward control (FFC) strategy is proposed for the production of crystals with desired size and shape distributions properly dealing with the disturbance in the inflow solute concentration. We assume that the actuator limit on the rate of change of the jacket temperature is sufficiently high such that the crystallizer temperature can be changed instantaneously. We note that if the jacket temperature change is not instantaneous, it will take an additional time for the PFC temperature to reach a desired profile, and as a result the system may lead to the production of crystals with undesired size and shape distributions over the time required for the PFC temperature to reach the desired profile:

1. Initially, we compute a set of optimal jacket temperatures ($T_{w,1}, T_{w,2}, T_{w,3}, T_{w,4}, T_{w,5}$) and an optimal superficial flow velocity, v_z, for the initial solute concentration, C_i, and they are applied to the crystallizer until the change in the inflow solute concentration is measured (i.e., a disturbance is detected). In this step, the spatial temperature profile at the steady state is similar to the one for $t=4$ h in Fig. 4.
2. When the change in the solute concentration is measured at the entrance of the PFC, a set of new optimal jacket temperatures ($T_{w,1}^{\text{new}}, T_{w,2}^{\text{new}}, T_{w,3}^{\text{new}}, T_{w,4}^{\text{new}}, T_{w,5}^{\text{new}}$) is computed for the new inflow solute concentration, C_i^{new}, while the superficial flow velocity remains identical. Then, the old jacket temperature for zone 1 is immediately replaced with the new jacket temperature and, for zone 2 to zone 5, the jacket temperatures remain identical because the inflow with the new solute concentration, C_i^{new}, has not reached zone 2 to zone 5 yet. Thus, a set of resulting jacket temperatures becomes ($T_{w,1}^{\text{new}}, T_{w,2}, T_{w,3}, T_{w,4}, T_{w,5}$).
3. When the inflow with the new solute concentration, C_i^{new}, has reached zone 2, the old jacket temperature, $T_{w,2}$, is replaced with a new jacket temperature, $T_{w,2}^{\text{new}}$. Thus, a set of resulting jacket temperatures becomes ($T_{w,1}^{\text{new}}, T_{w,2}^{\text{new}}, T_{w,3}, T_{w,4}, T_{w,5}$) and it is maintained until the inflow with the new solute concentration, C_i^{new}, reaches zone 3. In this step, the spatial temperature profile at the steady state is similar to the one for $t=10$ h in Fig. 4.
4. This strategy continues until the inflow with a new solute concentration, C_i^{new}, reaches the entrance of zone 5, and it is the time when

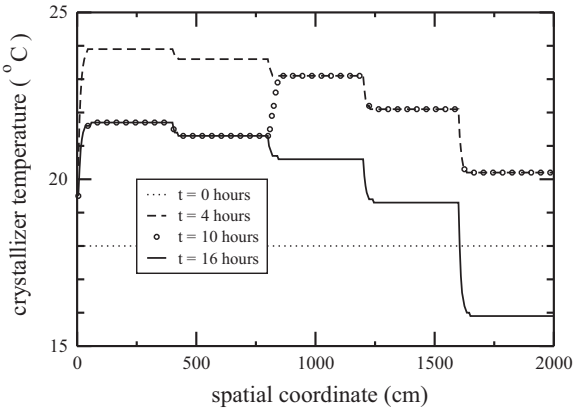

Fig. 4. The spatial evolution of the crystallizer temperature (T) at different times under FFC. The desired set-point values are $h_{110}=130$ μm and $\langle\alpha\rangle=0.85$ for the average crystal height in the direction of (110) face and crystal shape, respectively. The disturbance was introduced at $t=8.33$ h ($=30\,000$ s) when the inflow solute concentration was changed from $C_i=43$ to 34.4 mg/cm^3. It is noted that some of the data points for $t=10$ h have been excluded for clarity since they overlay with the data points for $t=4$ h.

a set of jacket temperatures becomes ($T_{w,1}^{new}, T_{w,2}^{new}, T_{w,3}^{new}, T_{w,4}^{new}, T_{w,5}^{new}$), which will be maintained for the rest of simulation. In this step, the spatial temperature profile at the steady state is similar to the one for $t=16$ h in Fig. 4.

5. If a new disturbance in the inflow solute concentration is detected, Step 1 to Step 4 will be repeated.

For example, a set of optimal jacket temperatures for the inflow solute concentration, $C_i = 43$ mg/cm^3, is presented in Fig. 5, which is applied to the PFC until a change in the inflow solute concentration is measured at $t=8.33$ h ($=30\,000$ s). Specifically, this disturbance to the system is modeled by decreasing the inflow solute concentration, C_i, from 43 to 34.4 mg/cm^3 at $t=30\,000$ s in the kMC simulations. Then, a set of new optimal jacket temperatures for the new inflow solute concentration $C_i^{new} = 34.4$ mg/cm^3 is computed, and applied for $8.33 < t < 14.16$ h according to the FFC strategy described above. For the production of crystals with desired size and shape distributions, the optimal superficial velocity $v_z=0.0763$ cm/s is computed for a given simulation time, $t_f=20$ h. In Table 1, a set of jacket temperatures at different times is presented for clarity. For $t > 14.16$ h, the inflow disturbance has reached zone 5 and as a result the set of old jacket temperatures has been completely replaced with a set of new jacket temperatures as is presented in Fig. 5. Owing to the FFC scheme, existing crystals that are in the middle or close to the outlet of the PFC can grow through the previous optimal jacket temperature profile, and as a result they are successfully produced with desired size and shape distributions. Furthermore, this FFC strategy only requires the measurement of the inflow solute concentration at the entrance of the PFC so it is robust to the inaccuracy of the online measurements. More results on the robust control of crystallization process can be found in the work by Chiu and Christofides (2000).

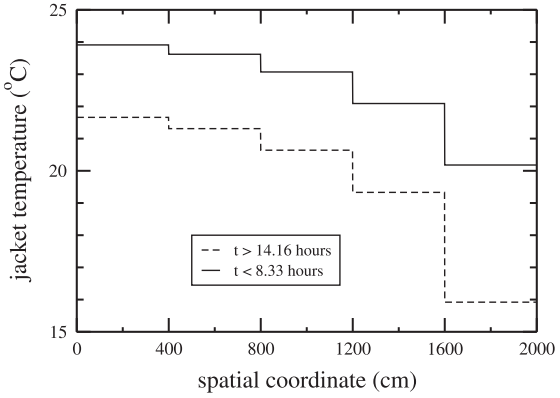

Fig. 5. The spatial profile of the jacket temperature (T_w) computed by solving MOP when the desired set-point values are $h_{110} = 130$ μm and $\langle\alpha\rangle = 0.85$ for the average crystal height in the direction of (110) face and crystal shape, respectively. To deal with the disturbance introduced to the inflow solute concentration, a set of new T_w values for $8.33 < t < 14.16$ h is updated according to the FFC strategy.

Table 1
A set of jacket temperatures at different times.

Time (h)	Jacket temperature (°C)				
	$T_{w,1}$	$T_{w,2}$	$T_{w,3}$	$T_{w,4}$	$T_{w,5}$
$(0 \le t < 8.33)$	23.91	23.62	23.07	22.09	20.18
$(8.33 \le t < 9.79)$	21.66	23.62	23.07	22.09	20.18
$(9.79 \le t < 11.24)$	21.66	21.31	23.07	22.09	20.18
$(11.24 \le t < 12.70)$	21.66	21.31	20.64	22.09	20.18
$(12.70 \le t < 14.16)$	21.66	21.31	20.64	19.33	20.18
$(14.16 \le t < 20)$	21.66	21.31	20.64	19.33	15.92

Remark 4. The proposed optimization/control approach can be extended to account for crystal agglomeration and/or breakage events by constructing moment models that capture the dominant dynamic behaviors of the agglomeration and breakage processes within the crystallization process.

Remark 5. As a complementary strategy to the proposed FFC scheme, a set of proportional-integral-derivative (PID) control schemes can be implemented for each zone to make slight adjustments to the optimal jacket temperatures (for a given crystallizer feed) and is used to suppress the effect of unmodeled disturbances/modeling uncertainty through the use of real-time online measurements of the size and shape distributions of the crystals of the PFC outlet stream.

6. Simulation results of continuous plug flow crystallizer

Continuous PFC processes have been traditionally operated at steady states. However, there is a limitation in the steady-state model in which it cannot describe a transient behavior of the system when there is a disturbance such as an abrupt change in the inflow solute concentration during the steady-state operation of the PFC. To this end, we have developed a dynamic model in Section 2 that describes the spatio-temporal evolution of system variables including the average crystal volume and shape, the number of crystals, and the solute concentration and the crystallizer temperature. In this work, we work at 4%(w/v) NaCl and pH=4.5. In Fig. 6, the solute concentration profile obtained from the dynamic model employed in the kMC simulation at different times proceeds gradually and eventually it reaches the steady state at $t \simeq 26\,500$ s.

The constant supersaturation control (CSC) strategy is one of the most widely used operating strategies for the operation of the crystallization processes in the industry. Furthermore, the controller performance of using a CSC strategy in batch processes can be close to that of the model predictive control (MPC) if the desired supersaturation level is chosen appropriately. For the PFC, however, it is rather difficult to maintain a constant supersaturation level because the solute concentration drops along the spatial coordinate of the crystallizer. Thus it requires a design of a particular spatial temperature profile to compensate the concentration drop, which is not possible without using a steady-state/dynamic model. In addition to the spatial supersaturation profile, the size distribution of the crystals produced from the PFC depends on the total length of the PFC. Therefore, using the model-free CSC scheme does not guarantee the production of crystals with desired size and shape distributions simultaneously.

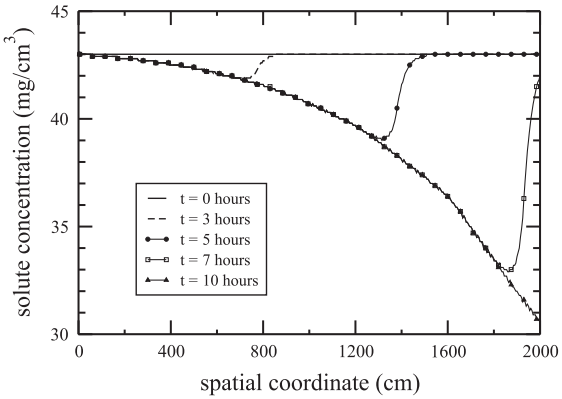

Fig. 6. The spatial evolution of the protein solute concentration level (C) at different times when there is no disturbance. The desired set-point values are $h_{110} = 130$ μm and $\langle\alpha\rangle = 0.85$ for the average crystal height in the direction of (110) face and crystal shape, respectively.

In this work, however, the production of the crystals with both desired size and shape distributions is achieved by applying the set of optimal jacket temperatures and the superficial flow velocity computed by solving the MOP (cf. Eq. (12)) according to the proposed FFC strategy to deal with the change (i.e., disturbance) in the inflow solute concentration. All simulations are performed in parallel using Message Passing Interface (MPI) to make use of heightened computational and memory requirements for this continuous crystallization process. The desired set-point value, $\langle\alpha\rangle = 0.85$, is chosen for the crystal shape because of the desire to work in a zone where the nucleation rate is negligible (i.e., metastable regime). Also, the set-point of $\langle h_{110}\rangle = 130\ \mu m$ is chosen for the crystal size in the direction of (110) face. As presented in Figs. 7 and 8, the effect of the disturbance is sufficiently suppressed and as a result the average crystal size in the direction of the (110) face and the average crystal shape are successfully regulated to a set of desired values, respectively. Without the implementation of the proposed FFC scheme, as presented in Figs. 7 and 8, the effect of the disturbance cannot be sufficiently suppressed and as a result $\sim 30\%$ of the crystal products deviates from the desired set-point values. The optimal superficial flow velocity used in the kMC simulation is $v_z = 0.0763$ cm/s, and sets of the optimal jacket temperatures are (23.91, 23.62, 23.07, 22.09, 20.18) °C and (21.66, 21.31, 20.64, 19.33, 15.92) °C for $C_i = 43$ and $C_i = 34.4$ mg/cm^3, respectively.

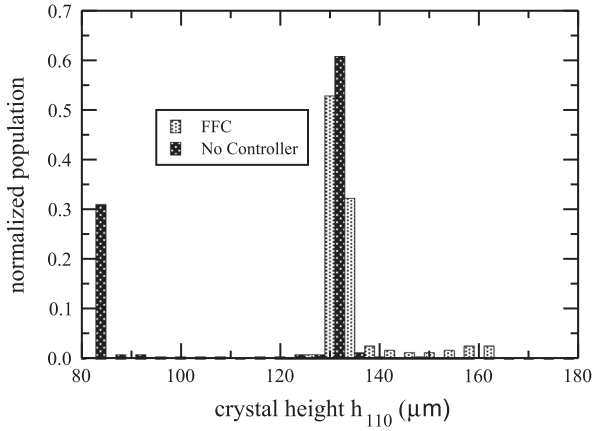

Fig. 7. The normalized crystal size distribution obtained from the kMC simulations under the FFC scheme is compared with that under no control scheme. The jacket temperatures computed by solving the MOP are applied to the PFC, and these crystals are collected throughout the PFC. The desired set-point values are $h_{110} = 130\ \mu m$ and $\langle\alpha\rangle = 0.85$ for the average crystal height in the direction of (110) face and crystal shape, respectively.

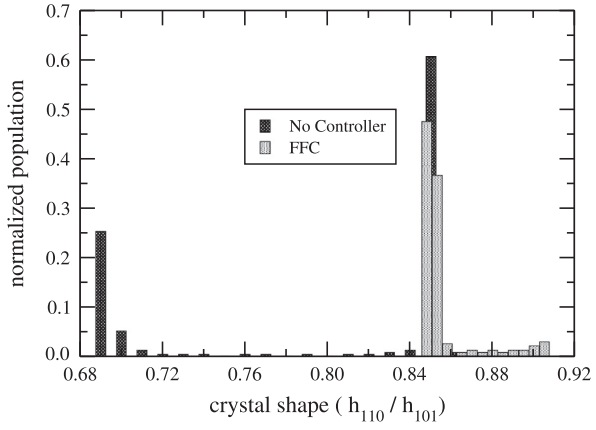

Fig. 8. The normalized crystal shape distribution obtained from the kMC simulations under the FFC scheme is compared with that under no control scheme. The jacket temperatures computed by solving the MOP are applied to the PFC, and these crystals are collected throughout the PFC. The desired set-point values are $h_{110} = 130\ \mu m$ and $\langle\alpha\rangle = 0.85$ for the average crystal height in the direction of (110) face and crystal shape, respectively.

The spatio-temporal profiles of the solute concentration, the crystallizer temperature, and the supersaturation level are presented in Figs. 9, 10 and 11, respectively. Because of the difference between a new jacket temperature profile computed for a new inflow solute concentration and the old jacket temperature profile, a set of discontinuous jumps is observed in Fig. 11. In Fig. 12, when the system is at a transient state at $t = 4$ h, the spatial profile of the solute concentration is determined by the combination of the neighboring steady-state profiles at $t = 0$ and $t = 8$ h, and a similar behavior is observed for another transient state at $t = 12$ h. The benefit of this discontinuity in the jacket temperature is that we can avoid the unnecessary temperature change for those crystals which are quite far from the disturbance and there is no need to change the jacket temperature for those crystals. As a result,

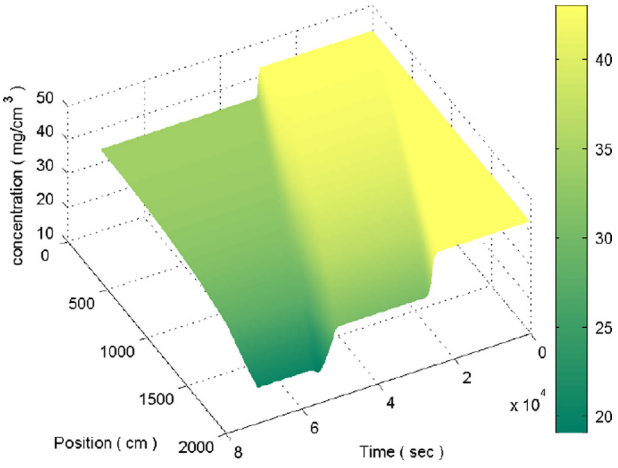

Fig. 9. The spatio-temporal evolution of the protein solute concentration level obtained from the kMC simulations in response to the disturbance introduced to the inflow solute concentration at $t = 8.33$ h ($= 30\,000$ s) when the solute concentration is changed from $C_i = 43$ to 34.4 mg/cm^3. A set of optimal jacket temperatures is obtained for the desired set-point values, $h_{110} = 130\ \mu m$ and $\langle\alpha\rangle = 0.85$, for the average crystal height in the direction of (110) face and crystal shape, respectively. Note that the origin, $(z, t) = (0, 0)$, is at the upper left of the position axis.

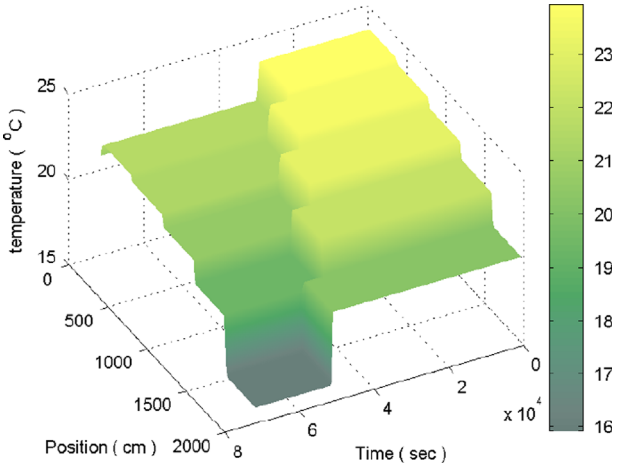

Fig. 10. The spatio-temporal evolution of the crystallizer temperature obtained from the kMC simulations in response to the disturbance introduced to the inflow solute concentration at $t = 8.33$ h ($= 30\,000$ s) when the solute concentration is changed from $C_i = 43$ to 34.4 mg/cm^3. The desired set-point values are $h_{110} = 130\ \mu m$ and $\langle\alpha\rangle = 0.85$ for the average crystal height in the direction of (110) face and crystal shape, respectively. Note that the origin, $(z, t) = (0, 0)$, is at the upper left of the position axis.

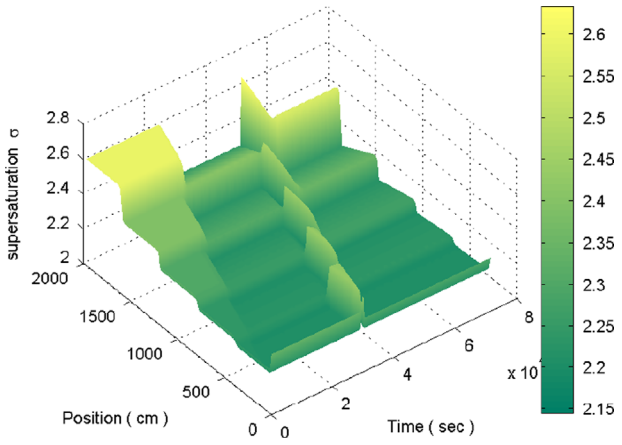

Fig. 11. The spatio-temporal evolution of the supersaturation level obtained from the kMC simulations in response to the disturbance introduced to the inflow solute concentration at $t=8.33$ h ($=30\,000$ s) when C_i is changed from 43 to 34.4 mg/cm^3. The desired set-point values are $h_{110}=130\,\mu$m and $\langle\alpha\rangle=0.85$ for the average crystal height in the direction of (110) face and crystal shape, respectively.

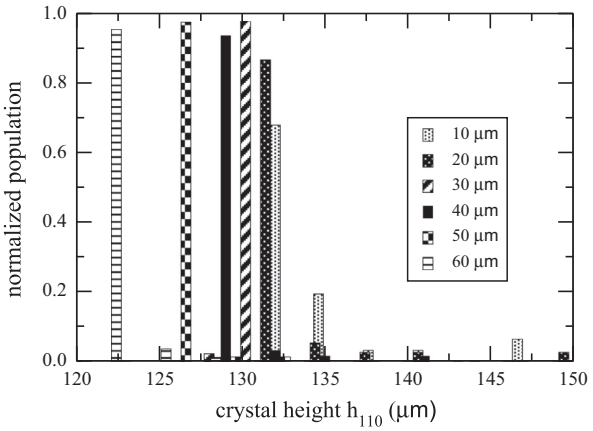

Fig. 13. The normalized crystal size distribution obtained from the kMC simulations for seed crystals with different heights, 10, 20, 30, 40, 50, 60 μm, in the direction of (110) face where the shapes of these crystal seeds are all cubical. For each run, the jacket temperatures computed by solving the MOP are applied to the PFC, and these crystals are collected throughout the PFC. The desired set-point values are $h_{110}=130\,\mu$m and $\langle\alpha\rangle=0.85$ for the average crystal height in the direction of (110) face and crystal shape, respectively.

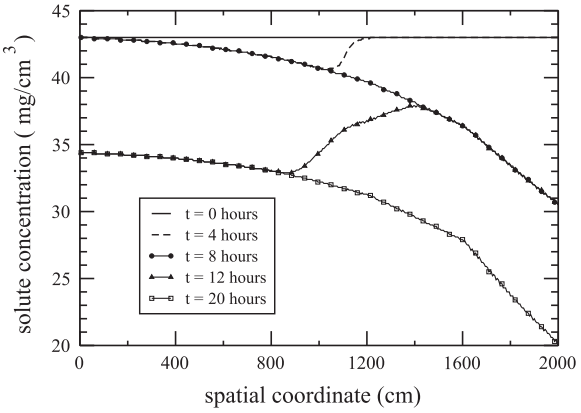

Fig. 12. The spatial evolution of the protein solute concentration level (C) at different times under FFC. The desired set-point values are $h_{110}=130\,\mu$m and $\langle\alpha\rangle=0.85$ for the average crystal height in the direction of (110) face and crystal shape, respectively. The disturbance was introduced at $t=8.33$ h ($=30\,000$ s) when the inflow solute concentration was changed from $C_i=43$ to 34.4 mg/cm^3.

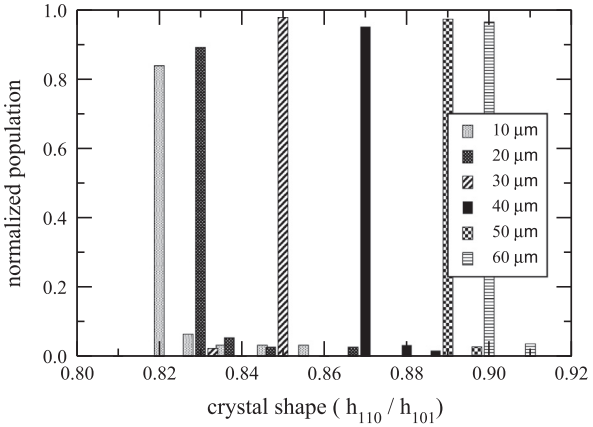

Fig. 14. The normalized crystal shape distributions obtained from the kMC simulations for seed crystals with different heights, 10, 20, 30, 40, 50, 60 μm, in the direction of (110) face where the shapes of these crystal seeds are all cubical. For each run, the jacket temperatures computed by solving the MOP are applied to the PFC, and these crystals are collected throughout the PFC. The desired set-point values are $h_{110}=130\,\mu$m and $\langle\alpha\rangle=0.85$ for the average crystal height in the direction of (110) face and crystal shape, respectively.

crystals with a desired size and shape distribution can be produced while the crystallizer is in a transient state.

The sensitivity of the size and shape of the crystals produced at the outlet of the PFC on the size of the initial seed crystals has also been investigated. Specifically, crystal size and shape distributions obtained from the kMC simulations for monodisperse seed crystals with different heights, 10, 20, 30, 40, 50, 60 μm, in the direction of the (110) face have been reported in Figs. 13 and 14, respectively. The weighting coefficients of the two objective functions used are $w_1=0.085$ and $w_2=1$. In Fig. 13, it is presented that the average size of the crystals obtained by applying the jacket temperatures computed from the MOP becomes smaller than the desired set-point if the seed crystals are large while the small seed crystals can grow to a desired product size. In Fig. 14, the shape of the crystals produced from large crystal seeds deviates from a desired set-point value than that of crystals produced from small crystal seeds. For larger crystal seeds, they have to grow considerably to reach the desired size, and as a result the solute concentration is dropped to a regime where the production of crystals with a relatively low crystal shape is achieved. We want to note that for a different crystal seed size a set of appropriate weighting factors, w_1 and w_2, would need to be found to properly drive crystal shape and size to desired set-point values, respectively.

In conclusion, the proposed FFC scheme along with the optimal solution obtained by solving the MOP can successfully drive the average size and shape of the crystal population produced from the PFC to desired set-point values. Additionally, the effect of change in the inflow concentration that occurred during the steady-state operation is suppressed by the proposed FFC, and, owing to the absence of back-mixing in the PFC, the production of crystals with a very narrow size distribution (i.e., low polydispersity) is achieved. Lastly, the number of segments in the PFC can be easily extended if it is necessary for the better performance of the proposed FFC scheme.

7. Conclusions

In this work, we first modeled the plug flow crystallization process where crystals grow from the seeds through kMC simulations. In general, a continuous PFC is operated at a steady state, and thus the steady-state model is typically used to describe the spatial profile of the important system variables, however, it cannot describe the transient behavior of the PFC. To this end, a dynamic model was developed to describe the spatio-temporal evolution of the number of crystals, the total crystal volume, the crystallizer temperature and the solute concentration, and the average crystal shape at a transient state as well as at a steady-state. Then, the method of moments was applied to the dynamic model to derive a reduced-order moments model which was used in the MOP to compute a set of optimal crystallizer jacket temperatures and superficial flow velocity that minimizes the sum of the squared deviation of the average crystal shape and size throughout the PFC from the desired set-point values, respectively.

In particular, when the disturbance was introduced, a set of new optimal jacket temperatures for each crystallizer segment was computed by solving the MOP for a new inflow solute concentration, and applied to the kMC simulation through the proposed FFC scheme. As a result, the production of crystals with desired size and shape distributions is achieved while $\sim 30\%$ of the crystal products are off the desired set-point values when the disturbance in the inflow solute concentration is not handled through the proposed FFC scheme.

Acknowledgments

Financial support from the National Science Foundation (NSF), CBET-0967291, the Extreme Science and Engineering Discovery Environment (XSEDE), TG-CCR120003, and the NSF Graduate Research Fellowship, DGE-0707424, given to Michael Nayhouse are gratefully acknowledged.

Appendix

For the purpose of the derivation of the moment models (Appendix A), the characteristic curve (Appendix B), and the steady-state model (Appendix C), the volumetric growth rate is assumed to be size independent and is only a function of the supersaturation level, that is $G_{vol}(V,\sigma) \simeq G_{vol}(\sigma)$.

Appendix A. Derivation of the moment models

To begin with the derivation, we multiply V^j to Eq. (8):

$$\int_0^\infty V^j \frac{\partial n}{\partial t} + v_z \int_0^\infty \frac{\partial n}{\partial z} V^j \, dV + G_{vol} \int_0^\infty \frac{\partial n}{\partial V} V^j \, dV = \int_0^\infty B_{seed} \delta(V - V_0, z - z_0) V^j \, dV$$

By setting $M_j(z,t) = \int_0^\infty n(V,z,t)\, dV$ and switching the order of operations

$$\frac{\partial M_j}{\partial t} + v_z \frac{\partial M_j}{\partial z} + G_{vol} \left[n V^j \Big|_{V=0}^{V=\infty} - j \int_0^\infty n V^{j-1} \, dV \right] = B_{seed} V_0^j \delta(z - z_0)$$

because $n(V,z,t)$ goes to 0 as V goes to ∞, and $n(V,z,t) = 0$ when $V = 0$ since there is no nucleation inside the crystallizer. Lastly, by rearranging it, we obtain

$$\frac{\partial M_j}{\partial t} = -v_z \frac{\partial M_j}{\partial z} + j G_{vol}(\sigma) M_{j-1} + B_{seed} V_0^j \delta(z - z_0) \tag{A.1}$$

where the terms $\partial M_j/\partial z$ and $B_{seed} V_0^j \delta(z - z_0)$ are associated with crystal seeding, which acts only at $z = z_0$ (i.e., it acts like an impulse), and thus their orders of magnitude are much higher than that of $(\partial M_j/\partial t)dz$ and $j G_{vol}(\sigma) M_{j-1}$. Therefore, integrating Eq. (A.1) from z_0^- to z_0^+ gives

$$0 = -v_z \int_{z_0^-}^{z_0^+} \frac{\partial M_j}{\partial z} \, dz + B_{seed} \int_{z_0^-}^{z_0^+} V_0^j \delta(z - z_0) \, dz$$

as a result a boundary condition follows that

$$M_j(z,t)|_{z=z_0} = \frac{B_{seed}}{v_z} V_0^j \tag{A.2}$$

Therefore, Eq. (A.1) can be written as follows:

$$\frac{\partial M_j}{\partial t} = -v_z \frac{\partial M_j}{\partial z} + j G_{vol}(\sigma) M_{j-1}$$

with a boundary condition, Eq. (A.2).

Appendix B. The method of characteristics

The two characteristic ODEs are derived as follows: First of all, by taking the derivative of $n(V,z)$ with respect to an arbitrary characteristic s, it gives

$$\frac{dn}{ds} = \left(\frac{\partial n}{\partial V}\right)\frac{dV}{ds} + \left(\frac{\partial n}{\partial z}\right)\frac{dz}{ds} \tag{B.1}$$

But from Eq. (8), assuming that the growth rate is independent of size

$$\frac{\partial n}{\partial t} = \left(\frac{\partial n}{\partial V}\right) G_{vol} + \left(\frac{\partial n}{\partial z}\right) v_z \tag{B.2}$$

Comparing coefficients on Eqs. (B.1) and (B.2) gives the equations for the characteristic curve as follows:

$$\frac{dV}{ds} = G, \quad \frac{dz}{ds} = v_z \tag{B.3}$$

and thus

$$\frac{dV}{dz} = \frac{G_{vol}}{v_z}$$

which defines the characteristic curve in the V–z plane and it allows calculation of the crystal volume distribution at any location z in the plug flow crystallizer. We note that the population distribution along a characteristic curve is constant because $dn/ds = 0$ by Eqs. (B.1) and (B.2).

Appendix C. Balance equations at steady state

The solute concentration $C(z)$ at steady state can be computed by substituting Eq. (11) into Eq. (1) and has the following form:

$$C(z) = C_i - \frac{\rho_c G_{vol} M_0(0)}{v_z} z$$

In a similar way, by substituting Eq. (11) into Eq. (6) and since $T_{w,j}$ is a constant within each crystallizer segment, the crystallizer temperature $T(z)$ at steady state can be obtained as follows:

$$\frac{dT}{dz} + BT(z) = -A + BT_{w,k} \tag{C.1}$$

where $A = \rho_c \Delta H_c G_{vol} M_0(0)/\rho C_p v_z$ and $B = U_c a_c/\rho C_p v_z$. Since this is a first order ordinary differential equation, we can compute the solution $T(z)$ by multiplying an integrating factor e^{Bz} to Eq. (C.1) as follows:

$$e^{Bz}\left(\frac{dT}{dz} + BT(z)\right) = (-A + BT_{w,k}) e^{Bz}$$

by grouping the left-hand side and integrating yields

$$\int d(e^{Bz}T(z)) = (-A+BT_{w,k})\int e^{Bz}\,dz$$

and applying the boundary condition for $T(z)$ at $z=0$ gives

$$e^{Bz}T(z) = (-A+BT_{w,k})\frac{1}{B}e^{Bz}\Big|_0^z + T_0$$

and it follows that

$$T(z) = \left(T_{w,k}-\frac{A}{B}\right)(1-e^{-Bz}) + T_0 e^{-Bz}$$

References

Alvarez, A., Myerson, A., 2010. Continuous plug flow crystallization of pharmaceutical compounds. Cryst. Growth Des. 10, 2219–2228.

Alvarez, A., Singh, A., Myerson, A.S., 2011. Crystallization of cyclosporine in a multistage continuous MSMPR crystallizer. Cryst. Growth Des. 11, 4392–4400.

Besenhard, M., Hohl, R., Hodzic, A., Eder, R., Khinast, J., 2014. Modeling a seeded continuous crystallizer for the production of active pharmaceutical ingredients. Cryst. Res. Technol. 49, 92–108.

Cacioppo, E., Pusey, M.L., 1991. The solubility of the tetragonal form of hen egg white lysozyme from pH 4.0 to 5.4. J. Gryst. Growth 114, 286–292.

Chiu, T., Christofides, P.D., 2000. Robust control of particulate processes using uncertain population balances. AIChE J. 46, 266–280.

Cogoni, G., Widenski, D., Grosso, M., Baratti, R., Romagnoli, J., 2014. A qualitative comparison between population balances and stochastic models for non-isothermal antisolvent crystallization processes. Comput. Chem. Eng. 63, 82–90.

Durbin, S.D., Feher, G., 1986. Crystal growth studies of lysozyme as a model for protein crystallization. J. Cryst. Growth 76, 583–592.

Durbin, S.D., Feher, G., 1991. Simulation of lysozyme crystal growth by the Monte Carlo method. J. Cryst. Growth 110, 41–51.

Eder, R., Schmitt, E., Grill, J., Radl, S., Gruber-Woelfler, H., Khinast, J., 2011. Seed loading effects on the mean crystal size of acetylsalicylic acid in a continuous-flow crystallization device. Cryst. Res. Technol. 3, 227–237.

Ferguson, S., Morris, G., Hao, H., Barrett, M., Glennon, B., 2013. Characterization of the anti-solvent batch, plug flow and MSMPR crystallization of benzoic acid. Chem. Eng. Sci 104, 44–54.

Ferguson, S., Morris, G., Hao, H., Barrett, M., Glennon, B. Automated self seeding of batch crystallizations via plug flow seed generation. Chem. Eng. Res. Des. http://www.dx.doi.org/10.1016/j.cherd.2014.01.028, in press.

Ferguson, S., Ortner, F., Quon, J., Peeva, L., Livingston, A., Trout, B., Myerson, A., 2014. Use of continuous MSMPR crystallization with integrated nanofiltration membrane recylce for enhanced yield and purity in API crystallization. Cryst. Growth Des. 14, 617–627.

Gnoth, S., Jenzsch, M., Simutis, R., Luubert, A., 2007. Process analytical technology (PAT): batch-to-batch reproducibility of fermentation processes by robust process operational design and control. J. Biotechnol. 132, 180–186.

Graham, M., Rawlings, J., 2013. Modeling and Analysis Principles for Chemical and Biological Engineers. Nob Hill Pub.

Griffin, D.W., Mellichamp, D.A., Doherty, M.F., 2010. Reducing the mean size of API crystals by continuous manufacturing with product classification and recycle. Chem. Eng. Sci. 65, 5770–5780.

Hou, G., Power, G., Barrett, M., Glennon, B., Morris, G., Zhao, Y., 2014. Development and characterization of a single stage mixed-suspension mixed-product-removal crystallization process with a novel transfer unit. Cryst. Growth Des. 14, 1782–1793.

Kalani, A., Christofides, P.D., 2002. Simulation, estimation and control of size distribution in aerosol processes with simultaneous reaction, nucleation, condensation and coagulation. Comput. Chem. Eng. 26, 1153–1169.

Kalbasenka, A., Spierings, L., Huesman, A., Kramer, H., 2007. Application of seeding as a process actuator in a model predictive control framework for fed-batch crystallization of ammonium sulphate. Part. Part. Syst. Charact. 24, 40–48.

Kwon, J.S., Nayhouse, M., Christofides, P.D., Orkoulas, G., 2013. Modeling and control of protein crystal shape and size in batch crystallization. AIChE J. 59, 2317–2327.

Kwon, J.S., Nayhouse, M., Christofides, P.D., Orkoulas, G., 2014. Modeling and control of crystal shape in continuous protein crystallization. Chem. Eng. Sci. 107, 47–57.

Kwon, J.S., Nayhouse, M., Orkoulas, G., Christofides, P.D. Enhancing crystal production rate and reducing polydispersity in continuous protein crystallization. Ind. Eng. Chem. Res. http://dx.doi.org/10.1021/ie5008163, in press.

Liu, J.J., Ma, C.Y., Hu, Y.D., Wang, X.Z., 2010. Effect of seed loading and cooling rate on crystal size and shape distributions in protein crystallization—a study using morphological population balance simulation. Comput. Chem. Eng. 34, 1945–1952.

Majumder, A., Nagy, Z., 2013. Fines removal in a continuous plug flow crystallizer by optimal spatial temperature profiles with controlled dissolution. AIChE J. 59, 4582–4594.

Mesbah, A., Landlust, J., Huesman, A., Kramer, H., Jansens, P., Van den Hof, P., 2010. A model-based control framework for industrial batch crystallization processes. Chem. Eng. Res. Des. 88, 1223–1233.

Miller, S.M., Rawlings, J.B., 1994. Model identification and control strategies for batch cooling crystallizers. AIChE J. 40, 1312–1327.

Patience, D.B., Rawlings, J.B., 2001. Particle shape monitoring and control in crystallization processes. AIChE J. 47, 2125–2130.

Ridder, B., Majumder, A., Nagy, Z., 2014. Population balance model based multi-objective optimization of a Multi-Segment Multi-Addition (MSMA) continuous plug flow antisolvent crystallizer. Ind. Eng. Chem. Res. 53, 4387–4397.

Schall, C., Arnold, E., Wiencek, J., 1996. Enthalpy of crystallization of hen egg-white lysozyme. J. Cryst. Growth 165, 293–298.

Sen, M., Singh, R., Ramachandran, R., 2014. Simulation-based design of an efficient control system for the continuous purification and processing of active pharmaceutical ingredients. J. Pharm. Innov. 9, 65–81.

Shi, D., Mhaskar, P., El-Farra, N.H., Christofides, P.D., 2005. Predictive control of crystal size distribution in protein crystallization. Nanotechnology 16, S562–S574.

Vetter, T., Burcham, C., Doherty, M.F., 2014. Regions of attainable particle sizes in continuous and batch crystallization processes. Chem. Eng. Sci 106, 167–180.

Wang, L., Lee, M.H., Barton, J., Hughes, L., Odom, T.W., 2008. Shape-control of protein crystals in patterned microwells. J. Am. Chem. Soc. 130, 2142–2143.

Worlitschek, J., Mazzotti, M., 2004. Model-based optimization of particle size distribution in batch-cooling crystallization of paracetamol. Cryst. Growth Des. 4, 891–903.

Yang, G., Kubota, N., Sha, Z., Louhi-Kultanen, M., Wang, J., 2006. Crystal shape control by manipulating supersaturation in batch cooling crystallization. Cryst. Growth Des. 6, 2799–2803.